Mon. Not. R. Astron. Soc. **000**, 000–000 (2000)

Cold gas and star formation in a merging galaxy sequence

Antonis Georgakakis[1⋆], Duncan A. Forbes[1,2†], Ray P. Norris[3‡]

[1] *School of Physics and Astronomy, University of Birmingham, Edgbaston, Birmingham, B15 2TT, UK*
[2] *Astrophysics & Supercomputing, Swinburne University, Hawthorn, VIC 3122, Australia*
[3] *Australia Telescope National Facility, CSIRO, Epping, NSW, Australia*

8 June 2000

ABSTRACT

We explore the evolution of the cold gas (molecular and neutral hydrogen) and star-formation activity during galaxy interactions, using a merging galaxy sequence comprising both pre- and post-merger candidates. Data for this study come from the literature but supplemented by some new radio observations presented here. Firstly, we confirm that the ratio of far-infrared luminosity to molecular hydrogen mass ($L_{FIR}/M(H_2)$; star-formation efficiency) increases close to nuclear coalescence. After the merging of the two nuclei there is evidence that the star-formation efficiency declines again to values typical of ellipticals. This trend can be attributed to $M(H_2)$ depletion due to interaction induced star-formation. However, there is significant scatter, likely to arise from differences in the interaction details (e.g. disk-to-bulge ratio, geometry) of individual systems. Secondly, we find that the central molecular hydrogen surface density, Σ_{H_2}, increases close to the final stages of the merging of the two nuclei. Such a trend, indicating gas inflows due to gravitational instabilities during the interaction, is also predicted by numerical simulations. Furthermore, there is evidence for a decreasing fraction of cold gas mass from early interacting systems to merger remnants, attributed to neutral hydrogen conversion into other forms (e.g. stars, hot gas) and molecular hydrogen depletion due to on-going star-formation. The evolution of the total-radio to blue-band luminosity ratio, reflecting the total (disk and nucleus) star-formation activity, is also investigated. Although this ratio is on average higher than that of isolated spirals, we find a marginal increase along the merging sequence, attributed to the relative insensitivity of disk star-formation to interactions. However, a similar result is also obtained for the nuclear radio emission, although galaxy interactions are believed to significantly affect the activity (star-formation, AGN) in the central galaxy regions. Nevertheless, the nuclear-radio to blue-band luminosity ratio is significantly elevated compared to isolated spirals. Finally, we find that the FIR–radio flux ratio distribution of interacting galaxies is consistent with star-formation being the main energising source.

Key words: Galaxies: mergers – galaxies: starburst – radio continuum: galaxies

1 INTRODUCTION

Tidal interactions and mergers are believed to play a significant role in the evolution of galaxies. Such phenomena can not only enhance the activity in and around the nuclear region (star-formation or AGN) but can also irreversibly alter the morphological appearance of the participant galaxies. Toomre & Toomre (1972) were the first to demonstrate that gravitational interactions can give rise to tidal features (e.g. bridges, tails) and also proposed the merging of disk galaxies as a plausible formation scenario for ellipticals (called the merger hypothesis). Indeed, recent more sophisticated numerical simulations have shown that dynamical friction and violent relaxation during disk-galaxy interactions will disrupt any pre-existing disks leading to relaxed $r^{1/4}$–law light profiles similar to those of ellipticals (Barnes 1988, 1992; Hernquist 1992, 1993). The same gravitational instabilities can produce significant gas inflows towards the centre of the galaxy, where enhanced star-formation activity is likely to take place (e.g. Mihos & Hernquist 1996).

Indeed, high molecular gas densities have been observed in the central regions of the IRAS starburst galax-

⋆ age@star.sr.bham.ac.uk
† forbes@star.sr.bham.ac.uk
‡ rnorris@atnf.csiro.au

ies, thought to be gas rich systems close to the final stages of merging (Kennicutt 1998; Planesas et al. 1997; Sanders & Mirabel 1996). The high molecular gas density regions are also found to be associated with enhanced nuclear star-formation (and/or AGN) activity as inferred from their far-infrared (FIR; Kennicutt 1998), radio (Hummel 1981; Hummel et al. 1990) and optical emission-line luminosity (Keel et al. 1985). A smaller but systematic enhancement compared to isolated spirals is also seen in the disk radio power (Hummel 1981) and disk Hα emission (Kennicutt et al. 1987) which is again attributed to interaction induced star-formation activity. Additionally, the fraction of interacting systems found in IRAS-selected samples increases with FIR luminosity (Lawrence 1989; Gallimore & Keel 1993), suggesting that collisions play a major role in triggering powerful starbursts.

Evidence also exists linking merger remnants with elliptical galaxies. For example, merger remnants tend to have optical and/or near–infrared light profiles that follow the $r^{1/4}$–law (Joseph & Wright 1985). Secondly, many, otherwise 'normal' ellipticals, exhibit low surface brightness loops and shells (Malin & Carter 1980; Schweizer & Seitzer 1988) that are likely to be due to past disk-galaxy encounters. Recently, Forbes, Ponman & Brown (1998) showed that late stage disk-disk mergers and ellipticals with young stellar populations deviate from the fundamental plane of ellipticals. This can be understood in terms of a centrally located starburst induced by a gaseous merger event.

The significance of tidal interactions in the evolution of galaxies has motivated a number of studies aiming to explore the properties of interacting systems at different stages during the encounter. Toomre (1977) first proposed a merging sequence of eleven peculiar galaxies spanning a range of post- to pre-mergers (the 'Toomre sequence') and suggested that the final product of the interaction is likely to resemble an elliptical galaxy. Keel & Wu (1995) used morphological criteria to define a merging galaxy sequence by assigning a merger stage number to each galaxy pair or merger remnant. They found that indicators of on-going star-formation activity, such as the $U-B$, $B-V$ colours and the FIR–to–blue-band luminosity ratio tend to peak close to the final stages of nuclear coalescence and then decrease at post-merger stages to attain values typical of ellipticals. A similar result was obtained by Casoli et al. (1991) who also studied the evolution of star-formation activity estimators (FIR temperature, FIR–to–blue-band luminosity, FIR luminosity to molecular hydrogen mass) for a small merging galaxy sequence defined by morphological criteria. More recently, Gao & Solomon (1999) used the projected separation between the nuclei of merging FIR-selected galaxies as an estimator of the interaction stage. They found clear evidence for increasing star-formation efficiency (SFE; estimated by the ratio of FIR-luminosity to molecular hydrogen mass) with decreasing nuclei separation. They argue that this is primary due to the depletion of the molecular gas reservoirs of these systems by on-going star-formation triggered by interactions. Hibbard & van Gorkom (1996) studied the cold gas properties and the dynamics of a small sample of pre- and post-mergers from the Toomre sequence. They find striking differences in the distribution of H I in pre- and post-mergers, with increasing fractions of H I outside the optical bodies at later stages. They argue that during the interaction about half of the cold gas material is ejected in tidal features, whereas the atomic gas remaining within the original disks is either converted into stars or heated up to X-ray temperatures. Read & Ponman (1998) investigated the X-ray evolution of a similarly defined merging sequence. Although they also found a rise and fall in the X-ray–to–blue-band luminosity around nuclear coalescence, the increase is by a factor of ten smaller than that seen in the FIR–to–blue-band luminosity. They argue that this is likely to be due to superwinds blowing out the hot X-ray emitting gas. These studies clearly indicate that large changes occur in the energetic, structural and kinematic properties of galaxies during interactions and mergers.

The above mentioned studies either concentrated only on pre-mergers (e.g. Gao & Solomon 1999) or investigated the properties of small samples of pre- and post-merger galaxies (assumed to be representative), albeit in great detail (Hibbard & van Gorkom 1996; Casoli et al. 1991; Read & Ponman 1998). In this paper we have compiled a large sample of interacting systems from the literature spanning a wide range of pre- and post-merger stages, aiming to explore the evolution of both their star-formation and their cold gas (molecular and neutral hydrogen) properties. Additionally, comparison of the galaxy properties along the merger sequence with those of 'normal' ellipticals and isolated spirals allows investigation of the merging hypothesis for the formation of ellipticals.

In section 2 we discuss the sample selection, while section 3 describes the new radio observations carried out for a selected sample of interacting galaxies. Section 4 presents the results from our analysis. Finally, in section 6 we summarise our conclusions. Throughout this paper we assume a value $H_o = 75\,\mathrm{km\,s^{-1}\,Mpc^{-1}}$.

2 THE SAMPLE

Compiling a sample of interacting galaxies and merger remnants from the literature is problematic. Different authors have used different selection criteria (e.g. FIR, morphological selection) that are likely to introduce biases against certain types of interactions. In this study, we merged several interacting galaxy samples from the literature, with different selection criteria in an attempt to minimise any selection biases. However, it should be noted that most of the galaxies in this study are FIR luminous and are also biased against mergers occurring along our line of sight. Therefore, although the present sample is by no means statistically complete, it could be regarded as representative of interacting systems and merger remnants spanning a wide range of properties. Our sample is largely culled from the following studies:

(i) Keel & Wu (1995) selected nearby pre- and post-merger galaxies based on their optical morphology and ordered them into a sequence by assigning a dynamical 'stage' number to each galaxy pair or merger remnant.
(ii) Gao & Solomon (1999) and Gao et al. (1998) compiled samples of FIR-luminous and ultra-luminous galaxies with available CO(1-0) observations (providing an estimate of the available molecular hydrogen mass,

$M(H_2)$). These samples consist exclusively of pre-mergers.

(iii) Surace et al. (1993) presented a sample of merging galaxies, morphologically selected from the $60\mu m$ flux density limited IRAS Bright Galaxy Sample (Soifer et al. 1987).

We focus on interacting systems and merger remnants from the above mentioned samples satisfying the following criteria:

(a) $\delta r \lesssim (D_1 + D_2)/2$, where δr is the separation between the two nuclei of the merging galaxies and D_1, D_2 their major axis diameters. This selection criterion is similar to that employed by Gao & Solomon (1999).

(b) recessional velocities $v \lesssim 13\,000\,\mathrm{km\,s^{-1}}$, corresponding to a distance $\lesssim 170\,\mathrm{Mpc}$.

(c) far-infrared luminosities $L_{FIR} < 10^{12}\,L_\odot$.

(d) we only consider disk mergers by discarding pairs for which there is morphological evidence that at least one of the components is elliptical.

(e) we attempt to restrict our sample to 'major mergers'; i.e. mergers involving galaxies of similar mass, in view of their relevance to the formation of elliptical galaxies. Therefore, we only consider pairs in which the individual components have a B-band magnitude difference of less than 1.5 mag, corresponding to a mass ratio 1:4 (assuming the same mass-to-light ratio). Mergers involving higher mass ratios may merely puff-up the disk and/or perhaps enlarge the bulge, but will not completely rearrange the light profile of the galaxy. However, the B-band magnitudes are affected by star-formation and do not provide a sensitive estimator of the total mass of a system. Nevertheless, to the first approximation they should provide a rough estimate of the galaxy mass ratio that is sufficient for the purposes of this paper.

The sample employed in this study is presented in Table 1, which has the following format

1. galaxy names.

2. heliocentric distance, D, in Mpc, assuming $H_o = 75\,\mathrm{km\,s^{-1}\,Mpc^{-1}}$. No correction for the Local Group velocity or the Virgocentric flow has been applied. However, these corrections are not expected to modify the estimated distances by more than 10%. Moreover, in our analysis we consider ratios of observed quantities that are independent of distance.

3. total radio flux density at 1.4 GHz (20 cm; $S^{tot}_{1.4}$) in mJy. For most galaxies in the present sample $S^{tot}_{1.4}$ was obtained from Condon et al. (1991) and from the NRAO VLA Sky Survey (NVSS) catalogue (Condon et al. 1998).

4. galaxy 'age' parameter. Each galaxy is assigned an 'age' parameter, relative to the time of the merging of the two nuclei. Negative 'ages' are for pre-mergers while positive 'ages' correspond to merger remnants. For pre-mergers the 'age' is estimated by dividing the projected separation of the two nuclei, δr, by an (arbitrary) orbital decay velocity $v = 30\,\mathrm{km\,s^{-1}}$. It is clear that the 'age' parameter for pre-mergers is affected by projection effects or different interaction geometries. However, to the first approximation, it provides an estimate of the stage of the merging and allows plotting of pre- and post-mergers on the same scale. For post-mergers we adopt the evolutionary sequence defined by Keel & Wu (1995) using dynamical and morphological criteria. In particular, the 'age' parameter for these systems is calculated by multiplying the dynamical stage number, defined by Keel & Wu (1995), by the factor 4×10^8 yr. This conversion factor is found to be appropriate for the 3 merger remnants in the Keel & Wu sample with available spectroscopic estimates (i.e. NGC 2865, NGC 3921, NGC 7252; Forbes, Ponman & Brown 1998). It should be stressed that the 'age' parameter for both pre- and post-mergers does not represent an absolute galaxy age but is an indicator of the evolutionary stage of the interaction.

5. far-infrared luminosity in solar units ($L_\odot = 3.83 \times 10^{26}$ W)

$$L_{FIR} = 4\pi\, D^2 \times 1.4 \times S_{FIR}, \qquad (1)$$

where S_{FIR} is the FIR flux in $\mathrm{W\,m^{-2}}$ between 42.5 and $122.5\mu m$ (Sanders & Mirabel 1996)

$$S_{FIR}(\mathrm{W\,m^{-2}}) = 1.26 \times 10^{-14} \times (2.58 \times \mathrm{f_{60}} + \mathrm{f_{100}}), \qquad (2)$$

where f_{60} and f_{100} are the IRAS fluxes at 60 and $100\mu m$ respectively in Jansky. The scale factor 1.4 in equation (1) is the correction factor required to account principally for the extrapolated flux longward of the IRAS 100μm filter (Sanders & Mirabel 1996).

6. molecular hydrogen mass, $M(H_2)$, estimated from the CO(1-0) emission. The sources from which the CO(1-0) intensity measurements were obtained are given in Table 1. The conversion factor $N(H_2)/I_{CO} = 3 \times 10^{20}\,\mathrm{cm^{-2}\,(K\,km\,s^{-1})^{-1}}$, appropriate for molecular clouds in the Milky Way (Sanders, Solomon & Scoville 1984) was adopted. It should be noted that use of this conversion factor assumes that the mean properties of the molecular gas in distant galaxies (i.e. density, temperature and metallicity) are similar to those of the Milky Way. However, the molecular clouds of the interacting systems studied here are likely to have both higher densities and temperatures and different metallicities compared to those of the Milky Way. These effects are expected to modify the CO-to-$M(H_2)$ conversion factor for these galaxies. Indeed, a number of studies suggest that use of the standard Galactic conversion factor for starbursts overestimates their $M(H_2)$ (Maloney & Black 1988; Tinney et al. 1990; Solomon et al. 1997) and therefore a smaller CO-to-$M(H_2)$ factor is appropriate for these galaxies. Nevertheless, to facilitate comparison of our results with other studies we use the standard Galactic $N(H_2)/I_{CO}$ conversion factor. In any case the results can be interpreted in terms of CO luminosity (L_{CO}) rather than $M(H_2)$, since a constant scaling factor is used throughout.

7. neutral hydrogen mass, $M(HI)$. The H I masses are related to the H I integrated intensities, $F(H\,I)$ (measured in $\mathrm{Jy\,km\,s^{-1}}$), by

$$M_{H\,I}(M_\odot) = 2.356 \times 10^5 \times F(H\,I) \times (D/\mathrm{Mpc})^2. \qquad (3)$$

The sources from which the H I intensity measurements were obtained are also given in Table 1.

8. total B-band magnitude, B_T. This has been corrected for Galactic extinction but not for internal extinction. This is because the systems studied here have disturbed morphologies and are likely to have more dust than normal spirals. Therefore, any correction for internal extinction which is based on the galaxy morphology (like that introduced in the RC3 catalogue by de Vaucouleurs et al. 1991) is expected to be unreliable. In few cases, RC3 did not provide total B-

band magnitudes and instead we used the total magnitudes from the catalogue compiled by Garnier et al. (1996).

9. Central surface density of molecular hydrogen, Σ_{H_2}, in units of $M_\odot\,pc^{-2}$. This is calculated from high resolution CO(1-0) observations by dividing the (unresolved) flux within the synthesised beam by its area (in pc^2). A consequence of this definition is an increase of the linear size of the region enclosed by the synthesised beam with distance. However, to the first approximation, Σ_{H_2} is representative of the molecular gas concentration of different systems. The Σ_{H_2} for interacting systems and merger remnant candidates were mainly obtained from Kennicutt (1998) and Planesas et al. (1997).

10-12. Central radio flux density at 1.49 GHz (20 cm), 4.79 GHz (6 cm) and 8.44 GHz (3 cm) respectively, integrated within an aperture of ≈ 2 kpc diameter at the distance of the galaxy. We use high resolution radio maps available on NED (1.49 GHz: Condon et al. 1990; 8.44 GHz: Condon et al. 1991) as well as our own radio observations at 4.79 and 8.64 GHz (see section 3). Upper limits are 3σ estimates, where σ is the RMS noise within a beam.

13. Radio spectral index, α, derived from the central 2 kpc diameter aperture flux densities using the relation

$$\alpha = \log(S_{\nu_1}/S_{\nu_2})/\log(\nu_1/\nu_2) \quad (4)$$

3 NEW RADIO OBSERVATIONS

To explore the effect of gravitational encounters to the nuclear radio emission of on-going interacting systems and merger remnants we have complemented high resolution radio data in the literature with our own new radio observations of seven systems (NGC 6769/70, ESO 286-IG19, NGC 1487, ESO 034-IG11, NGC 7764A, ESO 138-IG29, ESO 341-IG04). Also two of these systems (ESO 034-IG11 and ESO 138-IG29) are ring galaxies, allowing us to comment on the radio properties of this class of encounters. Interactions that produce a ring system are somewhat different to the disk-galaxy interactions/mergers studied here. In this case the intruder galaxy makes a rapid near perpendicular approach to the disk of the primary galaxy. Unlike more planar interactions, the disk is little affected until the intruder passes through it. Such collisions produce merger remnants that are different from those resulting from disk-galaxy encounters and therefore we consider them separately from the main sample. In all the figures, ESO 034-IG11 and ESO 138-IG29 systems are plotted as post-mergers, although we differentiate them from the rest of the merger remnants with different symbols.

The new radio observations were carried out using the Australia Telescope Compact Array at 4.79 GHz (6 cm) and 8.64 GHz (3 cm) simultaneously. We alternated observations of the target galaxy and a phase calibrator throughout the observing run. Our observational parameters are given in Table 2. The same amplitude calibrator (1934–638) was observed with each galaxy, with an assumed flux density of 5.83 Jy at 4.79 GHz and 2.84 Jy at 8.64 GHz. The data were edited, calibrated and CLEANed using the AIPS software package. The typical half–power beam–width (HPBW) of the final images are ≈ 2 arcsec at 4.79 GHz and ≈ 1 arcsec at 8.64 GHz.

Because these observations and their analysis were optimised for studying the nuclear region, they are relatively insensitive to extended emission. We will therefore concentrate on the emission within the central 10 arcsec. Details on individual galaxies are given in Appendix *A*. Also shown in Appendix *A* are the radio contours at 4.79 GHz overlayed[§] on the optical images (from Digital Sky Survey) of the seven galaxies in Table 2 (Figures A1-A7).

4 RESULTS AND DISCUSSION

This section studies the evolution of estimators of the star-formation activity and the cold gas content of interacting systems as a function of the 'age' parameter. In particular, the significance of any correlations between these quantities, including upper limits, is investigated using the Spearman rank correlation analysis implemented in the ASURV package (LaValley, Isobe & Feigelson 1992; Isobe, Feigelson & Nelson 1986). Throughout this paper we assume that the independent parameter in the Spearman rank correlation test is 'age'.

4.1 Star-formation efficiency

The ratio $L_{FIR}/M(H_2)$ estimates the number of massive stars formed per molecular cloud and is thus, related to the integrated galaxy star-formation efficiency (SFE). The molecular gas mass is estimated from the galaxy CO(1-0) emission using the standard CO–to–$M(H_2)$ conversion factor (section 2) to facilitate comparison of our results with other studies. It should be noted however that the CO–to–$M(H_2)$ conversion factor is likely to vary, depending on the galaxy physical conditions (see discussion below). Therefore, the CO(1-0) emission is strictly estimating the CO mass rather than $M(H_2)$.

Figure 1 plots the SFE as a function of the galaxy 'age' parameter. As explained in section 2 negative 'ages' correspond to pre-merger stages, zero corresponds to nuclear coalescence, while positive 'ages' are for merger remnants. It is clear from Figure 1 that there is a trend of increasing SFE as the interaction progresses towards the final stages of nuclear coalescence. Indeed, we calculate a Spearman rank correlation coefficient $r = 0.68$, corresponding to a probability that the correlation arises by chance $P < 0.01\%$. At later stages, the situation is less clear due to the small number of systems with available CO measurements. Nevertheless, there is evidence that throughout the merger process the SFE starts at a level comparable to isolated spirals, peaks around nuclear coalescence and decreases at post-mergers to a level similar to that of normal ellipticals. Similarly, Gao & Solomon (1999) found an increase in the mean SFE of interacting galaxy pairs with decreasing nuclear separation. Moreover, Solomon & Sage (1988) found that strongly interacting and merging galaxies (i.e. galaxies exhibiting tidal features such as tails and bridges) have SFEs that are about an order of magnitude higher than that of isolated and weakly interacting galaxies.

[§] These images were produced using the KVIEW application from the KARMA software suite (Gooch 1995)

Table 1: The sample

NAMES	D (Mpc)	$S_{1.4}^{tot}$ (mJy)	age ($\times 10^8$yr)	L_{FIR} ($10^9 \times L_\odot$)	$M(H_2)$[a] ($10^8 \times M_\odot$)	$M(H_I)$[b] ($10^8 \times M_\odot$)	B_T (mag)	Σ_{H_2} ($M_\odot$ pc^{-2})	$S_{1.49}^{cen}$ (mJy)	$S_{4.85}^{cen}$ (mJy)	$S_{8.44}^{cen}$ (mJy)	α
NGC 520, ARP 157	30.4	179.9	-1.92	65.0	102.0[1]	70.0[1]	12.19	3.81				
NGC 1614, ARP 186	63.7	115.0	-0.65	260.0	112.0[1]	29.0[2]	13.41	3.72	82.0			
NGC 2418, ARP 165	67.4		8.80	<2.9			13.05					
NGC 2623, ARP 243	73.8	98.5	1.60	260.0	55.4[1]	>2.7[2]	13.91	2.87	84.1		32.1	-0.55
NGC 2865	35.0	<0.4	12.00	<0.6		11.0[3]	12.30					
NGC 2911, ARP 232	42.4	58.6	12.00	1.3		19.0[4]	12.42					
NGC 2914, ARP 137	42.0		7.20	<0.9		5.2[5]	14.03					
NGC 3256[c,d]	34.0	642.0	-0.29	220.0	117.0[2]		11.60	3.13		65.0	39.0	-0.85
NGC 3256A[c,d]	34.0									31.0	18.0	-0.91
NGC 3256B[c,d]	34.0									34.0	21.0	-0.81
NGC 3303, ARP 192	83.8	5.0	-1.27	5.5	<3.7[3]	46.0[6]	14.03					
NGC 3414, ARP 162	18.9	4.0	11.20	<0.3		1.0[7]	11.96					
NGC 3509, ARP 335	102.7	27.9	3.20	36.0		210.0[8]	13.35					
NGC 3690, MRK 171	41.6	658.0	-1.44	360.0	140.0[4]	>45.0[9]	11.98	4.05	250.2		80.6	-0.64
NGC 3690A	41.6								56.2		15.0	-0.75
NGC 3690B	41.6								194.0		80.6	-0.5
NGC 3921, ARP 224	77.8	9.4	6.40	<13.0	35.0[5]	51.0[1]	13.06	2.13				
NGC 4038/9, ARP 244	21.9	572.0	-2.55	46.0	62.6[2]	69.0[10]	10.19	3.20				
NGC 4038	21.9	255.0					10.86					
NGC 4039	21.9	206.0					11.03					
NGC 4194, ARP 160	33.4	102.0	0.80	50.0	12.4[1]		13.01		73.9			
NGC 4676, ARP 242	88.1	30.5	-3.76	52.0	87.2[6]	68.0[1]	12.87	2.53				
NGC 4676A	88.1						13.82					
NGC 4676B	88.1						13.46					
IC 883, ARP 193	93.3	103.6	-0.10	310.0	67.5[1]	>61.0[11]	14.40	3.95	70.5		28.6	-0.51
Mrk 273, UGC 08696	151.0	143.0	-0.24	970.0	168.0[1]		15.15	4.57	59.2		52.4	-0.06
NGC 6052, ARP 209	62.9	94.0	-0.52	57.0	82.3[7]	90.0[12]	13.34					
NGC 6052A	62.9											
NGC 6052B	62.9											
NGC 6090, UGC 10267	117.0	46.4	-1.34	200.0	128.0[1]	100.0[13]	15.74	3.48	15.2		2.8	-0.97
NGC 6090A	117.0								11.2		2.8	-0.79
NGC 6090B	117.0								4.0			
NGC 6240, UGC 10592	97.9	427.2	-0.32	460.0	184.0[1]	86.0[11]	13.51	4.11				
NGC 7252, ARP 226	62.5	<128.7	9.60	37.0	36.7[8]	35.0[1]	12.54	2.61				
NGC 7585, ARP 223	46.0		13.60	0.7		<67.0[14]	12.22					
NGC 7592, VV 731	97.7	69.2	-1.93	160.0	182.0[1]	120.0[2]	13.95		32.3			
NGC 7592A	97.7	32.9							21.9			
NGC 7592B	97.7	20.3							10.4			
NGC 7727, ARP 222	24.7	3.4	12.80	0.6	1.0[9]	5.0[4]	11.41					
NGC 3597	46.5	67.8	-0.28	60.0	25.0[10]		13.39					
ESO 286-IG19[d]	171.2	31.0	6.00	690.0	148.0[11]	<35.0[15]	14.65			10.5	8.2	-0.41
NGC 1487[d]	11.3		-0.46	<1.0	0.1[12]	13.0[15]	12.34			1.0	<0.9	<-0.17
ESO 341-IG04[d]	80.8	<2.5	12.00	19.0	24.3[12]	40.0[15]	13.27			0.2	<1.4	<3.29

Table 1: continued

NAMES	D (Mpc)	$S_{1.4}^{tot}$ (mJy)	age ($\times 10^8$yr)	L_{FIR} ($10^9 \times L_\odot$)	$M(H_2)^a$ ($10^8 \times M_\odot$)	$M(H_I)^b$ ($10^8 \times M_\odot$)	B_T (mag)	Σ_{H_2} ($M_\odot$ pc^{-2})	$S_{1.49}^{cen}$ (mJy)	$S_{4.85}^{cen}$ (mJy)	$S_{8.44}^{cen}$ (mJy)	α
ESO 034-IG11[d]	88.1		1.80	32.0	46.8[13]	27.9[16]	13.27			0.2	0.4	1.17
NGC 6769/70[d]	50.8		-9.18	20.0			11.75			1.7	1.0	-0.89
NGC 6770[d]	50.8						12.66			1.7	1.0	-0.89
NGC 6769[d]	50.8						12.55					
NGC 7764A[d]	122.2		-9.28				30.33					
NGC 7764A NED2[d]	122.2						15.35			2.5	2.0	-0.37
NGC 7764A NED1[d]	122.2						14.98			0.3	<1.5	<2.72
ESO 138-IG29[d]	61.8		≈1.00				12.43			0.2	<1.5	<3.41
ESO 138-IG30[d]	61.8						13.61					
ARP 302, UGC 09618	134.7	72.4	-8.85	310.0	768.0[14]	>220.0[12]	14.01	2.60	16.1		3.8	-0.82
ARP 302A	134.7				670.0[14]		15.17					
ARP 302B	134.7				110.0[14]		14.37					
NGC 6670, UGC 11284	115.3	66.6	-4.87	267.0	550.0[4]	130.0[13]	14.98	2.48				
UGC 2369	124.7	50.0	-4.28	268.0	340.0[4]	>19.0[17]		3.08	34.8		8.8	-0.78
UGC 2369A	124.7								28.5			
UGC 2369B	124.7								6.3			
ARP 055, UGC 04881	157.1	31.6	-3.50	350.0	269.0[1]	190.0[2]	14.63	3.11	10.7		7.3	-0.21
VV 114, IC 1623	80.2	221.0	-1.96	310.0	510.0[15]	50.0[13]	14.27	3.81				
NGC 5256, MRK 266	111.4	159.0	-1.57	210.0	210.0[16]		13.89	>3.11	45.2			
NGC 5256A	111.4								21.6			
NGC 5256B	111.4								23.6			
IRAS 01077-1707	133.9	41.3	-7.42	270.0	400.0[4]		14.87		14.6			
IRAS 01418+1651	109.7	41.7	-1.44	300.0	69.2[1]	>17.0[12]	15.97		32.8		16.3	-0.39
IRAS 02114-0456	120.8	47.4	-1.70	180.0	258.0[4]	100.0[2]	14.70					
IRAS 03359+1523	141.5	19.4	-2.25	250.0	242.0[1]		15.82					
IC 2545	136.3	13.6	-1.08	320.0	105.0[17]	110.0[18]	14.76					
IRAS 13001-2339	85.9	59.8	-0.85	210.0	73.2[11]		14.49					
UGC 8335, ARP 238	123.2	53.1	-4.08	330.0	123.0[1]	<29.0[2]	14.20		39.4		16.7	-0.48
UGC 8335A	123.2	8.5							33.5			
UGC 8335B	123.2	44.6							5.9			
IC 4395, UGC 09141	146.0	29.0	-1.37	150.0	191.0[4]	65.0[13]	14.67					
MRK 848, VV 705	160.7	46.8	-1.57	490.0	335.0[4]		15.20	>3	19.0		10.6	-0.33
MRK 848A	160.7	29.9							6.9		2.4	-0.6
MRK 848B	160.7	18.0							12.1		8.2	-0.21
II Zw 96	144.3	36.3	-2.52	520.0	287.0[4]	120.0[19]						
NGC 835/3, ARP 318	54.3	36.1	-5.16	45.0	75.7[17]	32.0[13]	12.47					
NGC 835	54.3				60.2[18]		12.91					
NGC 833	54.3				15.5[18]		13.69					
NGC 2799/8, ARP 283	24.1	71.6	-3.66	25.0	32.5[19]	25.0[20]	12.74		55.7			
NGC 2798	24.1				28.6[19]	12.0[20]	13.04					
NGC 2799	24.1				3.9[19]	13.0[20]	14.32					
NGC 3395/6, ARP 270	21.6	108.5	-2.87	9.7	10.2[20]	30.0[20]	11.74		14.0			
NGC 3395	21.6	80.4					12.40		8.5			

Table 1: continued

NAMES	D (Mpc)	$S_{1.4}^{tot}$ (mJy)	age ($\times 10^8$yr)	L_{FIR} ($10^9 \times L_\odot$)	$M(H_2)$[a] ($10^8 \times M_\odot$)	$M(H_I)$[b] ($10^8 \times M_\odot$)	B_T (mag)	Σ_{H_2} ($M_\odot$ pc^{-2})	$S_{1.49}^{cen}$ (mJy)	$S_{4.85}^{cen}$ (mJy)	$S_{8.44}^{cen}$ (mJy)	α
NGC 3396	21.6	28.1					12.60		5.5			
NGC 4568/7, VV 219	30.1	136.0	-3.72	46.0	166.0^{19}	54.0^{21}	11.09					
NGC 4468	30.1				112.0^{19}		11.67					
NGC 4467	30.1				53.5^{19}		12.05					
NGC 5257/8, ARP 240	90.6	75.5	-11.17	200.0		130.0^{2}	12.68		7.2			
NGC 5257	90.6						13.35		2.7			
NGC 5258	90.6						13.52		4.5			
NGC 5427/6, ARP 271	34.9	63.0	-7.97	34.0	47.0^{20}	110.0^{6}	11.56					
NGC 5257	34.9						11.85					
NGC 5258	34.9						12.60					
NGC 5929/30, ARP 90	33.2	108.0	-1.57	22.0	11.9^{16}	11.0^{22}	12.94		109.0	22.1		-1.36
NGC 5929	33.2	70.6					13.54		51.7	22.1		-0.72
NGC 5930	33.2	37.4					14.04		57.3			
NGC 5953/4, ARP 91	28.8	72.3	-1.93	21.0	27.0^{16}	15.0^{23}	12.49		40.2			
NGC 5953	28.8	59.3					13.21		32.7			
NGC 5954	28.8	13.0					13.61		7.5			
NGC 4922, UGC 08135	98.1	37.8	-3.72	120.0		$<14.0^{12}$	14.05		30.7			
NGC 5331, UGC 08774	132.1	19.3	-6.30	240.0		$<220.0^{12}$	14.00		9.4			
NGC 5018[e]	37.3	3.1	15.20	3.4	$<6.0^{21}$	6.2^{24}	11.47					

[a]CO references

1: Sanders et al. 1991; 2: Aalto et al. 1995; 3: Elfhag et al. 1996; 4: Gao & Solomon 1999; 5: Yun & Hibbard 1999; 6: Casoli et al. 1991; 7: Sage et al. 1993; 8: Andreani et al. 1995; 9: Crabtree et al. 1994; 10: Wiklind et al. 1995; 11: Mirabel et al. 1990; 12: Horellou et al. 1997; 13: Horellou et al. 1995; 14: Lo & Gao 1997; 15: Yun et al. 1994; 16: Maiolino et al. 1997; 17: Kazes et al. 1990; 18: Boselli et al. 1996; 19: Young et al. 1995; 20: Solomon & Sage 1988; 21: Huchtmeier 1995

[b]H I references

1: Hibbard et al. 1996; 2: Bushouse et al. 1987; 3: Schiminovich et al. 1994; 4: Roberts et al. 1991; 5: Bottinelli et al. 1980; 6: Theureau et al. 1998; 7: Huchtmeier 1997; 8: Heckman et al. 1983; 9: Stanford et al. 1989; 10: Huchtmeier et al. 1975; 11: Richter et al. 1994; 12: Mirabel & Sanders 1988; 13: Martin et al. 1991; 14: Eskridge et al. 1991; 15: Horellou et al. 1997; 16: Higdon & Wallin 1997; 17: Haynes et al. 1997; 18: Kazes et al. 1990; 19: Giovanelli & Haynes, 1993; 20: Davis & Seaquist 1983; 21: Cayatte et al. 1990; 22: Richter et al. 1991; 23: Martin 1998; 24: Huchtmeier et al. 1995

[c]High resolution radio data from Norris & Forbes 1995

[d]The central radio flux densities in columns 11 and 12 are estimated at frequencies 4.79 and 8.64 GHz respectively

[e]The age assigned to NGC 5018 has been estimated spectroscopically (Terlevich & Forbes 1999)

Table 2. Observational parameters

Galaxy	Obs. Date	Phase Calibrator	3cm Beam (arcsec^2)	3cm P.A. (deg)	3cm Noise (μJy)	6cm Beam (arcsec^2)	6cm P.A. (deg)	6cm Noise (μJy)
NGC 6769/70	1995 Dec. 10	1925–610	1.08 × 0.96	29.0	30	2.02 × 1.80	31.0	30
ESO286–IG19	1995 Dec. 10	2058–425	1.33 × 1.03	13.4	50	2.47 × 1.87	9.8	40
NGC 1487	1995 Dec. 11	0355–483	1.48 × 0.93	–15.1	30	2.84 × 1.71	–16.3	30
ESO034–IG011	1995 Dec. 12	0757–737	1.31 × 0.87	–66.5	30	2.37 × 1.55	–73.4	30
NGC 7764A	1998 Jan. 28	0008–421	1.80 × 1.17	18.9	50	3.25 × 2.11	18.0	42
ESO138–IG29	1998 Jan. 24	1718–649	1.44 × 1.10	87.8	50	2.56 × 1.99	87.1	46
ESO341–IG04	1998 Jan. 10	2106–413	1.84 × 1.27	27.4	47	3.38 × 2.22	23.4	37

It is also clear from Figure 1 that there is significant scatter in the SFE evolution of pre-mergers. This is likely to be partly due to projection effects. We attempt to compensate for these effects by averaging the data for pre-mergers in different 'age' bins. The bins have variable widths so that they all comprise similar number of points (≈ 10). The mean SFE and the standard error is then calculated within each bin. The results are also shown in Figure 1. It is clear that the mean SFE increases toward the final coalescence of the two nuclei.

However, the observed scatter in the SFE evolution of pre-mergers is also expected to be due to differences in the details of individual interactions (e.g. geometry, initial conditions, bulge-to-disk ratio). Mihos & Hernquist (1996) carried out numerical simulations to explore the effect of galaxy structure on the gas dynamics and evolution of starburst activity in mergers. They found that in the case of galaxies with dense central bulges significant gas inflows occur close to the final stages of merging. On the contrary, gas inflows and thus, the peak of star-formation in bulgless galaxies occur earlier in the interaction. As a result some of the gas in these systems is depleted at early stages and only a relatively weak starburst is expected during nuclear coalescence. As demonstrated in Figure 2, where we plot SFE against Σ_{H_2}, gas inflows and the resulting high central molecular gas surface density (Σ_{H_2}), appears to be associated with enhanced SFE. Unfortunately, morphological information for the pre-merger systems in the present sample is sparse, with most of them classified as peculiars or irregulars. Therefore, without further data it is difficult to explore trends in the SFE evolution with bulge-to-disk ratio. Moreover, the orbital dynamics of the encounter also play a role, albeit a modest one, in regulating the gas inflow and therefore the peak of star-formation activity (Mihos & Hernquist 1996). In particular, prograde encounters produce gas inflows at early stages, as opposed to retrograde ones, where the gas dissipation occurs close to the final stages of the interaction. To further explore this trend, kinematic information for the interacting systems in the present sample are required. Since interacting galaxies may have a range of bulge-to-disk ratios and different orbital dynamics, a scatter is expected in the evolution of their SFEs. Unfortunately, the present sample cannot be used to assess the relative importance of galaxy properties and interaction geometry in moderating the observed activity. The fact that the SFE of the present sample peaks close to nuclear coalescence (despite the scatter) indicates that systems with late gas inflows (i.e. bulge dominated galaxies in the Mihos & Hernquist (1996) scenario) are likely to be over-represented in our sample (Mihos 1999). A similar result is obtained by Gao & Solomon (1999) and Gao et al. (1998) who studied the SFE as a function of nuclear separation for FIR luminous galaxies (some of which overlap with the present sample). Therefore, it is probable that the FIR selection biases the sample towards systems with late gas inflows. Although the present sample also comprises morphologically selected galaxy pairs, most of the pre-merger galaxies are FIR-luminous.

Gao & Solomon (1999) argue that the observed increase in the SFE for close galaxy pairs is primarily due to the decreasing mass of available $M(H_2)$ as the interaction progresses to advanced stages. However, Solomon & Sage (1988) concluded that the elevated SFE of strongly interacting/merging galaxies in their sample (compared to isolated galaxies) is mainly due to higher FIR luminosities rather than low $M(H_2)$ masses (estimated by their CO luminosities). Figures 3 and 4 plot the FIR luminosity and molecular hydrogen mass as a function of the 'age' parameter respectively for the interacting systems in the present sample. We find no correlation between 'age' and L_{FIR}, with a Spearman rank correlation coefficient $r = 0.14$ and a probability for no correlation $P = 36\%$. On the contrary, an anti-correlation is found between 'age' and $M(H_2)$, albeit a weak one, with $r = -0.32$ and $P = 5\%$, in better agreement with Gao & Solomon (1999). In any case, the elevated SFE close to nuclear coalescence can be attributed to star-formation triggered off by the interaction process that efficiently converts the existing giant molecular clouds into stars (Gao & Solomon 1999; Solomon & Sage 1988). However, Solomon & Sage (1988) also argue that the observed high SFE in late interacting systems may arise from an underestimation of the $M(H_2)$ mass in these galaxies by the CO luminosity. In particular, in high density environments, similar to those expected in the nuclear regions of merging galaxies, the CO–to–H_2 conversion factor might be significantly higher than that in Galactic Giant Molecular Clouds (GMCs). Moreover, a metallicity lower than that of the Galactic GMCs would also significantly reduce the sensitivity of the CO emission to molecular hydrogen and thus result in underestimation of the $M(H_2)$ (Combes 1999 and references therein). Nevertheless, dynamical arguments suggest that the Galactic CO–to–H_2 conversion factor is likely to give close to correct or even underestimate H_2 masses, even in the extreme environments found in merging galaxies (Solomon & Sage 1988; Solomon et al. 1997; Downes et al. 1993). Additionally, the

fact that Figure 1 exhibits less scatter than that in Figures 3 and 4 implies that the increase in SFE close to nuclear coalescence in Figure 1 is likely to be real.

Additionally, it is also clear from Figures 3 and 4 that at later, post-merger times, the FIR luminosity decreases as the star-formation declines, while the molecular hydrogen is further depleted but at a slower rate. Consequently, the SFE of merger remnants declines after the merger event.

Also shown in Figure 1 are the typical SFEs for isolated spirals (Solomon & Sage 1988) and normal ellipticals (Lees et al. 1991). For ellipticals, the presence of few systems with high SFE in the Lees et al. (1991) sample biases the mean to large values. A more robust estimator of the central value of a distribution with a long tail is the median value. Additionally, the presence of $M(H_2)$ upper limits in the Lees et al. (1991) sample requires the use of survival analysis to estimate statistical quantities. The median SFE for ellipticals is therefore, estimated using the ASURV Rev. 1.2 code (Feigelson, Isobe & LaValley 1992), which implements the methods presented in Feigelson & Nelson (1985).

Early, well separated interacting systems have SFE comparable to that of isolated spirals, suggesting that these systems are in a pre-starburst stage (Lo, Gao & Gruendl 1997). Additionally, there is also evidence that the SFE of merger remnants and 'normal' ellipticals form a continuous decreasing sequence. However, CO(1-0) observations of a larger sample of merger remnant candidates is needed to further explore their association with ellipticals. Casoli et al. (1991) and Hibbard & van Gorkom (1996) also studied the evolution of the SFE of a small sample of pre- and post-merger. They found that post-mergers have SFE that closely resembles that of 'genuine' ellipticals, although they are relatively rich in cold gas (molecular and neutral hydrogen) compared to E/S0s. Nevertheless, Hibbard & van Gorkom (1996) argue that these merger remnants are likely to rid a large fraction of their gas within few Gyr, mainly due to modest on-going star-formation.

In Figure 1 there is evidence that the ring galaxy ESO 034-IG11 has lower SFE compared to merger remnant candidates produced by major disk-galaxy interactions. Horellou et al. (1995) also found a mean $SFE = 16 \pm 10\,\mathrm{L_\odot/M_\odot}$ for ring galaxies, suggesting that the star-formation activity in ring systems declines faster after the close approach of the intruder galaxy compared to disk-galaxy mergers. Alternatively, this might indicate that the encounters that give rise to ring systems do not produce as powerful starbursts as disk-galaxy mergers. Indeed, the star-formation activity in ring systems is mainly restricted in the ring (Higdon & Wallin 1997) due to the propagation of density waves, rather than the nuclear region as in disk-galaxy mergers. Therefore, the density waves triggered by head-on collisions are less likely to produce the high concentrations of molecular hydrogen found in the nuclear regions of the systems resulting from disk-galaxy encounters. As demonstrated in Figure 2, such high concentrations of molecular hydrogen are also associated with powerful starbursts.

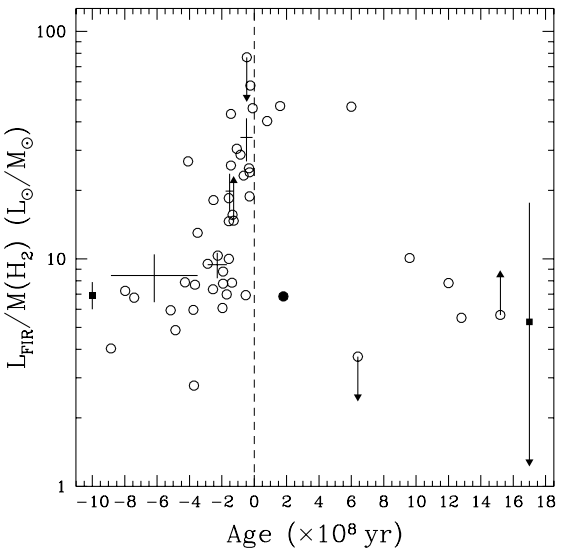

Figure 1. Star-formation efficiency ($SFE = L_{FIR}/M(H_2)$) as a function of the galaxy 'age' parameter. Negative 'ages' are for pre-mergers while positive 'ages' correspond to post-mergers. The dashed line signifies the time of nuclear coalescence ('age'=0) and separates pre- and post-merger systems. Open circles are the galaxies in the present sample. The filled circle represents the ring galaxy ESO 034-IG11. Filled squares correspond to the mean SFE for (i) isolated spirals (left; Solomon & Sage 1988) and (ii) ellipticals (right; Lees et al. 1991). The crosses signify the mean SFE for pre-mergers averaged within 'age'-parameter bins. The horizontal error bars represent the width of each bin, selected so that each bin comprises about 10 systems. The vertical error bars are the standard error on the mean SFE within each bin. There is evidence that the SFE starts at a level similar to that of isolated spirals, peaks at nuclear coalescence and then declines at post-merger stages to a level similar to that of normal ellipticals.

4.2 Molecular hydrogen surface density

The nuclear surface density of molecular hydrogen, Σ_{H_2}, is plotted as a function of the galaxy 'age' parameter in Figure 5. There is evidence for increasing Σ_{H_2} as the interaction progresses towards the final nuclear coalescence. Indeed, we find a Spearman rank correlation coefficient $r = 0.78$, corresponding to a probability that the observed trend arises by chance $P = 0.2\%$. However, there is significant scatter and the data are sparse, since there is still limited number of galaxies with high resolution CO(1-0) observations. An additional caveat is that the synthesised beam (i.e. the minimum resolving element) probes regions of different linear size for systems at different distances, contributing to the observed scatter.

As explained in the previous section, we attempt to compensate for projection effects by estimating the mean Σ_{H_2} within 'age' bins of variable width. The results are also shown in Figure 5, indicating an increase of the mean Σ_{H_2} for pre-mergers towards nuclear coalescence. A similar result was obtained by Gao et al. (1998) who investigated the evolution of Σ_{H_2} as a function of nuclear separation of interacting systems. Also shown in Figure 5 is the mean Σ_{H_2} for isolated spirals (Kennicutt et al. 1998). It is clear that the interacting systems have significantly higher Σ_{H_2} compared to isolated spirals. However, it should be noted that the molecular gas surface densities of isolated spirals are cal-

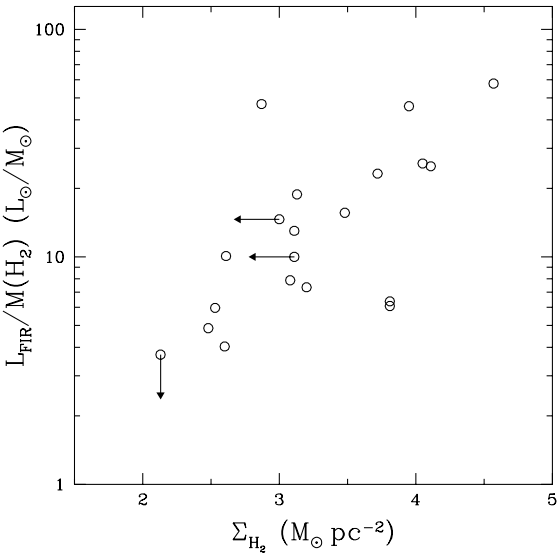

Figure 2. Star-formation efficiency as a function of central molecular gas surface density. There is evidence that the SFE and Σ_{H_2} are correlated, indicating that high central concentrations of molecular hydrogen are also associated with powerful starbursts.

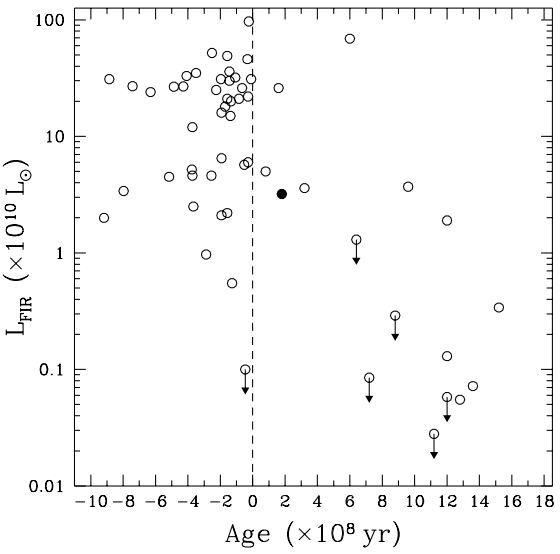

Figure 3. FIR luminosity, L_{FIR}, as function of the galaxy 'age' parameter. The points are the same as in Figure 1. The dashed line separates pre- and post-mergers. For pre-mergers there is no obvious trend between L_{FIR} and galaxy 'age'. However, the L_{FIR} at post-merger stages steeply decreases as the the interaction induced starburst declines.

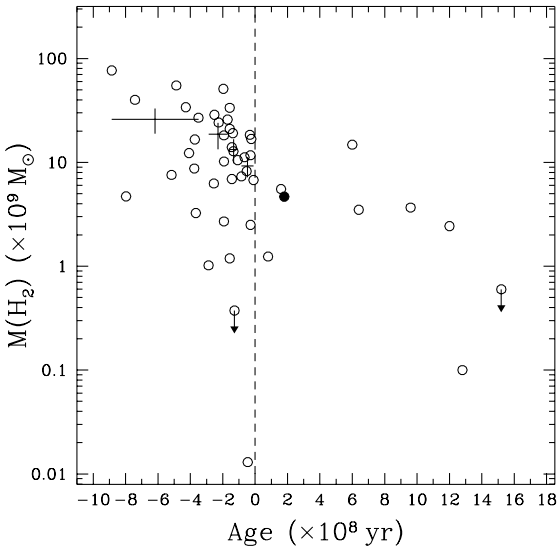

Figure 4. Molecular hydrogen mass, $M(H_2)$, as function of the galaxy 'age' parameter. The points are the same as in Figure 1. The crosses signify the mean $M(H_2)$ for pre-mergers averaged within 'age'-parameter bins. The horizontal error bars represent the width of the bin, selected so that each bin comprises the same number of systems ($\approx$ 10). The dashed line separates pre- and post-mergers. There is evidence for a decrease in $M(H_2)$ along the merger sequence, likely to be due to $M(H_2)$ depletion by the interaction induced starburst.

culated by averaging the CO(1-0) emission over the optical radius of the galactic disk, rather than the nuclear region. Therefore, the Σ_{H_2} of field spirals calculated by Kennicutt et al. (1998) is expected to significantly underestimate their central surface density. We were also unable to find a representative average Σ_{H_2} for ellipticals in the literature.

Numerical simulations (e.g. Mihos & Hernquist 1996) have demonstrated that tidal encounters trigger significant gas in-flows that lead to high central concentrations of gas. However, as discussed in the previous section, these models also predict that gas dissipation occurs at different stages of the interaction depending on the galaxy internal structure and interaction geometry.

For post-mergers the situation is less clear, since there are only three merger remnants in our sample with available high resolution CO(1-0) observations and thus, any conclusions are hampered by poor statistics. Nevertheless, there is evidence for decreasing Σ_{H_2} as the system evolves after the nuclear coalescence. Observations of the molecular gas distribution of a statistically complete sample of merger remnants are essential to further explore this trend. Moreover, little is known about the molecular gas distribution of 'normal' elliptical galaxies. Comparison between the Σ_{H_2} for ellipticals and candidate merger remnants is essential to test this aspect of the merging hypothesis.

4.3 Cold gas

The ratio of cold (molecular and neutral hydrogen) gas mass to the blue band luminosity ($[M(HI)+M(H_2)]/L_B$) is plot-

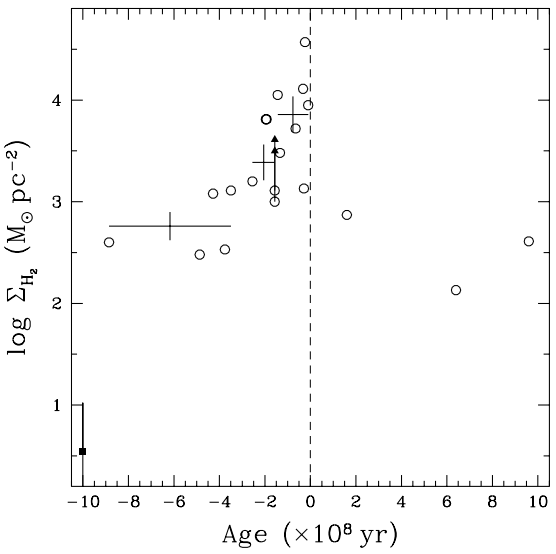

Figure 5. Central nuclear surface density of molecular hydrogen, Σ_{H_2}, as a function of the galaxy 'age' parameter. The points are the same as in Figure 1. The filled squares corresponds to the mean Σ_{H_2} of isolated spirals (Kennicutt 1998; however see discussion in text). The crosses signify the mean Σ_{H_2} for pre-mergers averaged within 'age'-parameter bins. The horizontal error bars represent the width of each bin, selected so that each bin comprises about 5 points. The vertical error bars are the standard error around the mean Σ_{H_2} within each bin. There is evidence that the Σ_{H_2} for pre-mergers peaks close to nuclear coalescence, indicating gas inflows arising from gravitational instabilities. At post-merger stages the Σ_{H_2} seems to decline but the poor statistics do not allow any firm conclusions to be drawn.

ted as a function of the 'age' parameter in Figure 6. This ratio estimates the fraction of cold gas mass in the system. There is evidence that $(M(HI)+M(H_2))/L_B$ is, on average, decreasing along the merging sequence from early interacting systems to late merger remnants, indicating cold gas depletion during the interaction. For post-mergers, we find that 'age' and $(M(HI) + M(H_2))/L_B$ are anti-correlated with a Spearman rank coefficient $r = -0.86$ and a probability that the distribution is uniform $P = 0.3\%$.

As explained in the previous section, gravitational instabilities during the interaction drive most of the gas into the centre of the system, where it is likely to be efficiently converted into stars. Additionally, Hibbard & Van Gorkom (1996) found little evidence for neutral hydrogen within remnant bodies, with most of it lying in the outer regions (i.e. tidal features). Numerical N-body simulations have shown that the gravitational forces experienced during the merger can force about half of the outer disc H I into a tail, the rest of the H I being forced into the inner regions (Hibbard & Mihos 1995). As less than a quarter of the total H I is found within these regions, Hibbard & Van Gorkom (1996) concluded that most of the centrally forced H I gas is converted during the merger into some other form. They propose that the gas has been turned into molecular gas, stars or has been heated up to X-ray temperatures, either through compression leading to cloud-cloud collisions or through energy input from massive stars and supernovae. The presence of Balmer absorption lines in the merger remnants NGC 7252 and NGC 3921 (Dressler & Gunn 1983; Schweizer 1996) is direct evidence that some of the original atomic gas is ultimately converted into stars. Searches for molecular hydrogen in these same galaxies have revealed that although they are gas rich compared to ellipticals or S0s, they have below average molecular gas content for their spirals progenitors (Solomon & Sage 1988; Young & Knezek 1989; Hibbard & van Gorkom 1996), indicating that any net conversion of atomic to molecular hydrogen is relatively inefficient. This is also demonstrated in Figure 7, where we plot the ratio of neutral to molecular hydrogen mass as a function of the 'age' parameter. It is clear that there is significant scatter without any obvious correlation, suggesting that the net conversion from H I to H_2 is not large during the merging. However, it should be noted that any conversion from H I to H_2 is likely to take place in the central galaxy regions, whereas Figure 7 plots the global gas properties of interacting systems.

Regarding the X-ray properties of mergers, Read & Ponman (1998) found an increase in the X-ray luminosity of galaxies close to the nuclear coalescence indicative of the presence of hot gas. However, they found little evidence for the presence of hot X-ray emitting gas in merger remnants. They concluded that this is likely to be due to galactic winds, similar to those observed in the nearby starburst M 82, that blow the hot gas out of the system.

Elliptical galaxies are also known to have little cold gas. This is demonstrated in Figure 6 showing the mean $[M(HI)+M(H_2)]/L_B$ ratio for ellipticals (Bregman, Hogg & Roberts 1992). Although merger remnants are gas rich compared to normal ellipticals, they seem to form a sequence that supports the merger scenario as a possible formation mechanism for elliptical galaxies. Hibbard et al. (1994) studied the gas properties of the merger remnant NGC 7252 and found that although it is gas rich compared to ellipticals and S0s, it is likely to resemble these galaxies in few Gyrs. In particular, the H I is mostly found in the tidal tails, while the atomic gas content of the remnant body is typical to that of E/S0s. There is also some evidence for on-going conversion of the returning tidal tail H I into stars. Moreover, the molecular gas in the NGC 7252 is also likely to be depleted within the next few Gyrs, due to modest on-going star-formation.

The ring galaxy ESO 034-IG04 in Figure 1 has cold gas mass fraction similar to that of merger remnant candidates resulting from major disk-galaxy encounters. A similar result was obtained by Horellou et al. (1995), who found a mean $[M(HI) + M(H_2)]/L_B$ ratio of 0.22 ± 0.17 for ring systems.

4.4 Radio flux density

We define the ratio, R, between total radio (1.4 GHz) flux density, $S_{1.4}^{total}$ and B-band luminosity (Hummel 1981)

$$R = \log(S_{1.4}^{total}) + 0.4 \times (B_T - 12.5). \quad (5)$$

The R parameter is independent of distance and estimates the ratio between radio power and optical luminosity. It has been demonstrated that the mean radio power is proportional to the mean optical luminosity of galaxies (Hummel

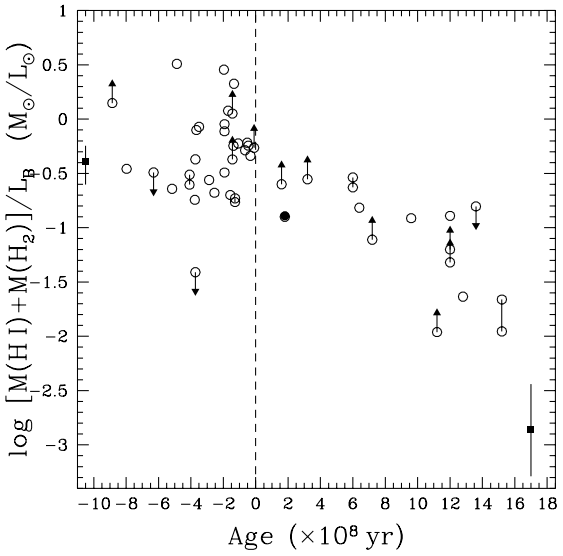

Figure 6. Total mass of neutral and molecular hydrogen normalised to the B-band luminosity as a function of galaxy 'age'. The points are the same as in Figure 1. Points connected with a line represent the upper and lower $[M(H_2) + M(HI)]/L_B$ limits for that system. For isolated spirals and ellipticals (filled squares) the mean $[M(H_2) + M(HI)]/L_B$ is taken from Young & Knezek (1989) and Bregman, Hogg & Roberts (1992) respectively. The filled circle is the ring system ESO 034-IG11. There is evidence for a decrease in $[M(H_2)+M(HI)]/L_B$ from pre- to post-mergers, likely to be due to cold gas depletion.

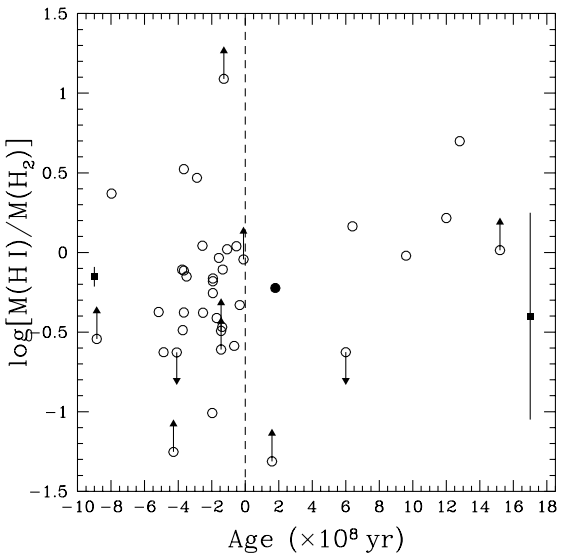

Figure 7. Neutral to molecular hydrogen mass, $M(HI)/M(H_2)$, as a function of galaxy 'age'. The points are the same as in Figure 1. For isolated spirals and ellipticals (filled squares) the mean $M(HI)/M(H_2)$ is taken from Young & Knezek (1989) and Wiklind et al. (1995) respectively. The filled circle is the ring system ESO 034-IG11. There is no obvious trend, implying little net conversion from H I to H_2 during the interaction (however see discussion in text).

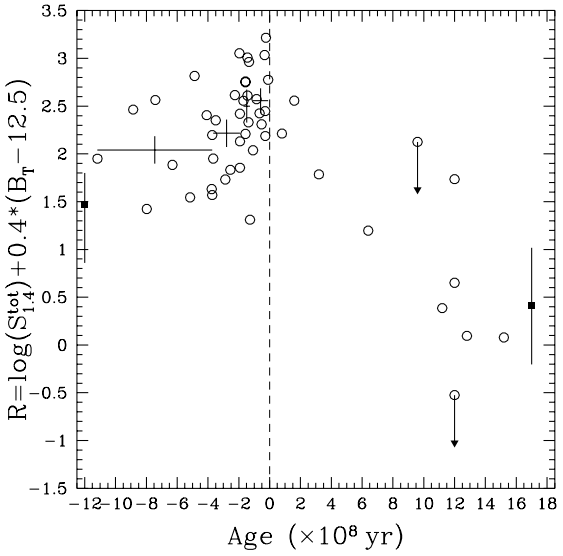

Figure 8. Total radio to B-band flux ratio ($R = \log S^{tot}_{1.4} + 0.4 \times [B_T - 12.5]$) as a function of galaxy 'age'. The points are the same as in Figure 1. The filled squares are the mean R for isolated spirals (Klein 1982) and ellipticals (Sadler 1984). The crosses signify the mean R for pre-mergers averaged within 'age'-parameter bins. The horizontal error bars represent the width of the bin, selected so that each bin comprises about 10 systems. The vertical error bars are the standard error on the mean. Although the mean R for pre-mergers is higher that that of isolated spirals, it marginally increases along the merger sequence towards the nuclear coalescence. The R parameter at post-merger stages declines steeply, to values typical of normal ellipticals.

1981). The R parameter also takes into account this effect, providing an estimate of the excess radio emission in galaxies due to star-formation or AGN activity.

The R parameter is plotted against the galaxy 'age' in Figure 8. For pre-mergers, we find a marginally significant correlation with Spearman rank coefficient $r = 0.41$ and a probability that the distribution is uniform $P = 1.3\%$. The mean R within different 'age' bins (of variable width) is also shown in the same figure. In agreement with our previous result the mean R parameter for pre-mergers, although on average higher than that of isolated spirals (≈ 0.8 dex; Klein 1982), marginally increases along the merging sequence towards the final stages of the tidal encounter. This is a surprising result since the radio flux is related to star-formation activity in galaxies (Condon et al. 1992 and references therein). This can be partly attributed to projection effects and differences in the details of individual interactions. Moreover, it has been shown that tidal encounters primarily act to increase the nuclear galaxy star-formation within the central kpc (Keel et al. 1985; Kennicutt et al. 1987) and only moderately affect the activity (i.e. star-formation) in the disk. In particular, Hummel (1981) found little difference between the disk radio power (normalised to the blue-band luminosity) of interacting pairs and isolated spirals. On the contrary an increase by a factor of 2.5 was found for the central radio power of the two samples. Also shown in Figure 8 is the mean R for ellipticals (Sadler

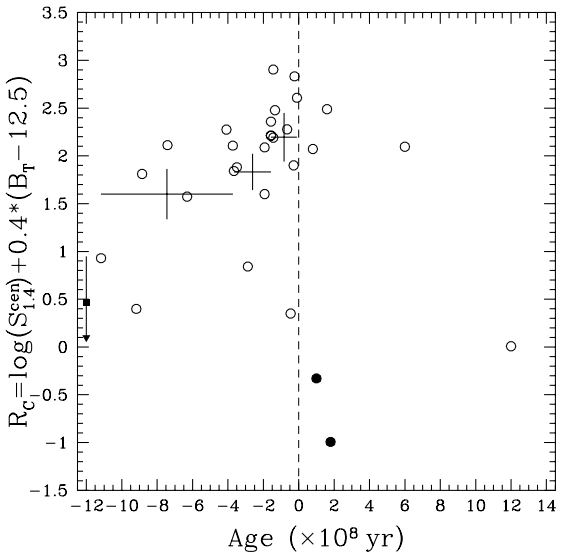

Figure 9. Central radio to the B-band flux ratio ($R_C = \log S_{1.4}^{cen} + 0.4 \times [B_T - 12.5]$) as a function of galaxy 'age'. The points are the same as in Figure 1. The filled square is the mean R_C for isolated spirals (Hummel 1981). The filled circles are the ring galaxies ESO 034-IG04 and ESO 138-IG29. The crosses signify the mean R for pre-mergers averaged within 'age'-parameter bins. The horizontal error bars represent the width of the bin, selected so that each bin comprises about 5 points. The standard error around the mean is shown by the vertical error bars. Although the mean R_C for pre-mergers is significantly higher that that of isolated spirals, it marginally increases along the merger sequence towards the nuclear coalescence. At post-merger stages there is evidence for a decline in the R_C but the poor statistics hamper any interpretation.

1984). It is clear that the radio properties of merger remnant candidates and ellipticals are in fair agreement.

To further explore changes in the central radio activity along the merging sequence, we estimate the 1.4 GHz radio flux density of the galaxies in the present sample within the central ≈ 2 kpc diameter region. For that purpose we employ high resolution radio data available on NED, mostly taken from Condon et al. (1991). For galaxies without available 1.4 GHz data, $S_{1.4}^{cen}$ is estimated from high resolution observations at other frequencies (8.4 GHz or 4.9 GHz), if available, assuming a power-law spectral energy distribution $S_\nu \propto \nu^{-\alpha}$. The radio spectral index is either taken to be 0.8 or calculated from the 8.4 GHz and 4.9 GHz radio flux densities, if available. The results are presented in Figure 9, plotting the central radio flux density to blue band luminosity, R_C, against galaxy 'age'. For pre-mergers, we find a Spearman rank coefficient $r = 0.55$ and a probability that the distribution is uniform $P = 0.9\%$, suggesting that 'age' and R_C are marginally correlated. Similarly, the increase in the mean R_C along the merger sequence for pre-mergers is marginal. However, the poor statistics do not allow any firm conclusions to be drawn. Nevertheless, the mean R_C of interacting systems is significantly elevated compared to that of isolated spirals (≈ 1.5 dex), in agreement with previous studies (Hummel 1981).

The ring galaxies ESO 034-IG11 and ESO 138-IG29 in Figure 9 have central radio to the B-band flux ratios significantly lower than merger remnants resulting from major disk-galaxy encounters. This is likely to be due to the fact that the star-formation in ring systems is concentrated in the ring rather than the nuclear region, due to density waves triggered by the nearly head-on collision.

5 THE FIR–RADIO CORRELATION

The logarithmic FIR–to–radio flux density ratio is defined by (Condon et al. 1991)

$$q = \log[(S_{FIR}/3.75 \times 10^{12})/S_{1.4}^{tot}], \quad (6)$$

where S_{FIR} is the FIR flux density (section 2, equation 2) and $S_{1.4}^{tot}$ is the total radio flux density (section 2) in units of $\mathrm{W\,m^{-2}\,Hz^{-1}}$. Radio and FIR selected starbursts as well as optically selected spiral and irregular galaxies exhibit a very narrow q-distribution ($\sigma_q \approx 0.2$) centred on $< q > \approx 2.34$. This tight distribution is attributed to star-formation activity resulting in both FIR emission and supernovae explosions, whose remnants emit at radio wavelengths via sychnotron radiation. Additionally, galaxies with radio emission powered by an AGN have, on average, $q < 2$, implying that the FIR–radio flux ratio can be employed, to the first approximation, to constrain the nature of the energising source (AGN/star-formation; Condon 1992 and references therein). However, discriminating between AGN and star-formation activity as the dominant energising source is not an easy task, especially in the case of dusty FIR-luminous systems. Nevertheless, recent studies suggest that mid-infrared spectroscopy can provide an efficient tool for classifying the energy source that dominates the observed activity (Genzel et al. 1998; Lutz et al. 1999; Rigopoulou et al. 1999).

Figure 10 plots q as a function of the galaxy age parameter. Also shown in this figure is the region occupied by starbursts and normal spirals. The interacting systems in the present sample (both pre- and post-mergers) have a mean FIR–radio flux ratio $< q >= 2.36 \pm 0.25$, in fair agreement with the canonical value of $q = 2.34 \pm 0.20$. Therefore, the q parameters of most of these systems are consistent with star-formation activity being the main energising source. There also few pre-mergers in the sample with $q < 2$, which might be indicating the presence of an AGN contributing to the observed activity. Interestingly, all these systems have nuclear separation $\delta r < 5$ kpc implying that they are likely to be at an advanced interaction stage, close to the final merger event. Nevertheless, the majority of the very close galaxy pairs ($\delta r < 5$ kpc) have FIR–radio flux ratios consistent with star-formation activity.

Smith et al. (1993) also investigated the FIR–radio correlation of interacting galaxies and concluded that star-formation is likely to be the main source responsible for the observed FIR and radio activity. Similarly, Bushouse et al. (1988) studied the FIR properties of interacting galaxies and concluded that it is not necessary to invoke mechanisms other than starbursts to account for their activity. Dahari (1985) used optical spectra to determine the nature of the energising source in interacting systems and found little evidence for an excess of Seyfert nuclei in paired galaxies compared to isolated spirals. Moreover, he found no Seyfert type

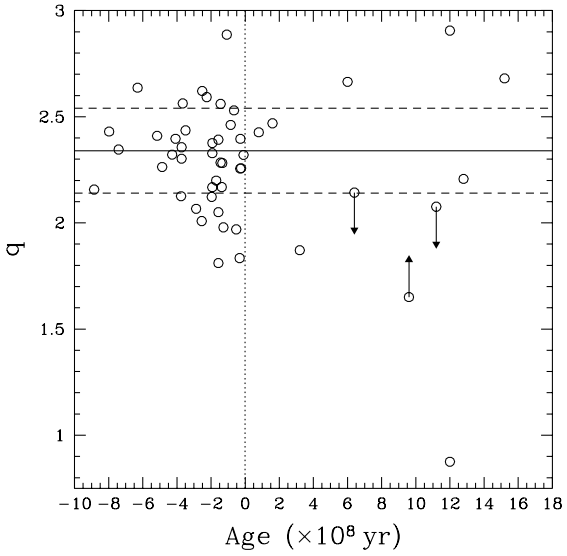

Figure 10. Logarithmic FIR–radio flux ratio, q, as a function of the galaxy age parameter. Open circles are the interacting galaxies studied here. The continuous line is the mean q for starbursts, while the dashed lines signify the 1σ envelope around the mean. The dotted line separates pre- from post-mergers. Most of the interacting galaxies are consistent with star-formation being their energising source.

spectra in a sub-sample of extremely distorted spirals (e.g. similar the majority of pre-mergers studied here). Genzel et al. (1998) and Rigopoulou et al. (1999) used mid-infrared spectroscopy to explore the nature of ultra-luminous infrared galaxies (ULIRGS), many of which are experiencing on-going interactions. They conclude that starburst activity dominates the bolometric luminosity of the majority of these extreme systems, although many of them also have an AGN component. Moreover, Rigopoulou et al. (1999) found no evidence for an increase in AGN-dominated ULIRGS with decreasing projected nuclear separation.

Merger remnant candidates in Figure 10 exhibit significant scatter, with many of them deviating from the expected relation for starbursts, although the poor statistics do not allow any firm conclusions to be drawn. Moreover, little is known about the FIR-radio flux ratio distribution of merger remnants. Nevertheless, elliptical galaxies, with which post-mergers are most likely associated, follow the FIR–radio relation for star-forming galaxies (Wrobel & Heeschen 1991). Nevertheless, a number of ellipticals are also found to deviate from this relation having low q values, indicating the presence of an AGN. Moreover, Wrobel & Heeschen (1991) also found that a fraction of the elliptical galaxies in their sample lied well above the canonical FIR-radio relation (high q values). They argue that these systems are likely to have extended low-surface brightness radio emission, associated with star-formation, that might remain undetected by the existing observations.

6 CONCLUSIONS

In this paper we compile a sample of interacting/merging galaxies aiming to study the evolution of the gas properties and star-formation along a galaxy merger sequence. The present sample, although not complete, is representative of interacting systems and merger remnants spanning a range of properties. Our conclusions are summarised below

(i) We find a statistically significant increase in the SFE of on-going mergers close to the final stages of nuclear coalescence. Nevertheless, there is significant scatter, attributed to both projection effects and differences in the interaction details of individual systems. The observed trend is likely to be due to $M(H_2)$ depletion by star-formation. At post-merger stages, despite the poor statistics, there is evidence that the SFE declines to values typical to ellipticals, in agreement with the merger hypothesis.

(ii) There is also strong evidence for increasing central surface density of molecular hydrogen close to nuclear coalescence, indicating gas dissipation due to gravitational instabilities. However, projection effects and differences in the interaction details of individual systems contribute to the observed scatter.

(iii) There is evidence for a decrease in cold gas mass fraction (neutral and molecular hydrogen) along the merging sequence. This attributed to H I conversion into other forms within the body of the system during the interaction and $M(H_2)$ depletion due to residual star-formation activity. This trend also seems to support the merging scenario for the formation of ellipticals.

(iv) The total radio power normalised to the blue-band luminosity, although higher than that of isolated spirals, marginally increases along the merger sequence. This is attributed to the fact that interactions mainly affect the nuclear galaxy activity, whereas there is moderate enhancement in the disk star-formation rate. However, a similar result is obtained for the central radio power of interacting systems (normalised to the blue-band luminosity). Nevertheless, the nuclear radio to blue-band luminosity ratio of interacting systems is significantly elevated compared to isolated spirals.

(v) The FIR–radio flux ratio distribution of interacting galaxies is consistent with star-formation being the main energising source. However, there is evidence that some systems might have an AGN contributing to the observed activity.

7 ACKNOWLEDGEMENTS

We thank Chris Mihos and the anonymous referee for valuable comments and suggestions. This research has made use of the NASA/IPAC Extragalactic Database (NED), which is operated by the Jet Propulsion Laboratory, Caltech, under contract with the National Aeronautics and Space Administration. The Australia Telescope is funded by the Commonwealth of Australia for operation as a National Facility managed by CSIRO. The Digitised Sky Survey was produced at the Space Telescope Science Institute under US government grant NAG W-2166.

REFERENCES

Aalto S., Booth R. S., Black J. H., Johansson L. E. B., 1995, A&A, 300, 369
Andreani P., Casoli F., Gerin M., 1995, A&A, 300, 43
Barnes J. E., 1988, ApJ, 331, 699
Barnes J. E., 1992, ApJ, 393, 484
Becker R. H., White R., L., Edwards A. L., 1991, ApJS, 75, 1
Bregman J. N., Hogg D. E., Roberts M. S., 1992, ApJ, 387, 484
Bergvall N., Johansson L., 1995, A&AS, 113, 499
Bergvall N., Ronnback J., Johansson L., 1989, A&A, 222, 49
Boselli A., Mendes De Oliveira C., Balkowski C., Cayatte V., Casoli F., 1996, A&A, 314, 738
Bottinelli L., Gouguenheim L., Paturel G., 1980, A&A, 88, 32
Bushouse H. A., 1987, ApJ, 320, 49
Bushouse A. H., Lamb S. A., Werner W. M., 1988, ApJ, 335, 74
Casoli F., Dupraz C., Combes F., Kazes I., 1991, A&A, 251, 32
Cayatte V., Balkowski C., van Gorkom J. H., Kotanyi C., 1990, AJ, 100, 604
Combes F., 1999, astro-ph/9910296
Condon J. J., 1992, ARA&A, 30, 575
Condon J. J., Huang Z. P., Yin Q. F., Thuan T. X., 1991, ApJ, 378, 65
Condon J. J., Helou G., Sanders D. B., Soifer B. T., 1990, ApJS, 73, 359
Condon, J. J., Cotton, W. D., Greisen, E. W., Yin, Q. F., Perley, R. A., Taylor, G. B., & Broderick, J. J. 1998, AJ, 115, 1693
Crabtree D. R., Smecker-Hane T., 1994, AAS, 185, 107.14
Dahari O., 1985, ApJS, 57, 643
Davis L. E., Seaquist E. R., ApJS, 53, 269
de Vaucouleurs G., de Vaucouleurs A., Corwin H.G., Buta R.J., Paturel G., Fouque P., 1991, Third Reference Catalogue of Bright Galaxies (Springer-Verlag: New York) (RC3)
Downes D., Solomon P. M., Radford S. J. E., 1993, ApJ, 414, L13
Dressler A., Gunn J. E., 1983, ApJ, 270, 7
Elfhag T., Booth R. S., Hoeglund B., Johansson L. E. B., Sandqvist A., 1996, A&AS, 115, 439
Eskridge P. B., Pogge R. W., 1991, AJ, 101, 2056
Feigelson E. D., Nelson P. I., 1985, ApJ, 293, 192
Feigelson E., Isobe T., La Valley M., 1992, Dept. Astron. & Astrophys. Pennsylvania State Univ. Pub. ASURV.
Forbes D. A., Ponman T. J., Brown R. J. N., 1998, 508, L43
Gallimore J. F., Keel W. C., 1993, AJ, 106, 1337
Gao Y., Solomon P. M., 1999, ApJ, 512, 99
Gao Y., Gruendl R. A., Hwang C. Y., Lo K. Y., astro-ph/9812459
Garnier R., Paturel G., Petit C., Marthinet M. C., Rousseau J., 1996, A&AS, 117, 467
Genzel R., Lutz D., Sturm E., Egami E., Kunze D., Moorwood A. F. M., Rigopoulou D., Spoon H. W. W., Sternberg A., Tacconi-Garman L. E., Tacconi L., Thatte N., 1998, ApJ, 498, 579
Giovanelli R., Haynes M. P., 1993, AJ, 105, 1251
Gooch R. E., "Karma: a Visualisation Test-Bed", in Astronomical Data Analysis Software and Systems V, ASP Conf. series vol. 101, ed. G. H. Jacoby and J. Barnes, ASP, San Francisco, p. 80, ISSN 1080-7926
Haynes M. P., et al. 1997, AJ, 113, 1197
Heckman T. M., Balick B., van Breugel W. J. W., Miley G. K., 1983, AJ, 88, 583
Hernquist L., ApJ, 1992, 400, 460
Hernquist L., ApJ, 1993, 409, 548
Hibbard J. E., Guhathakurta P., van Gorkom J. H., Schweizer F., 1994, AJ, 107, 67
Hibbard J. E., van Gorkom J. H., AJ, 1996, 111, 655
Hibbard J. E., Mihos J. C., 1995, AJ, 110, 140
Higdon J. L., Wallin J. F., 1997, ApJ, 474, 686
Horellou C., Booth R., 1997, A&AS, 126, 3
Horellou C., Casoli F., Combes F., Dupraz C., 1995, A&A, 298, 743
Hummel E., Van der Hulst J. M., Kennicutt R. C., Keel W. C., 1990, A&A, 236, 333
Hummel E., 1981, A&A, 96, 111
Huchtmeier W. K., Sage L. J., Henkel C., 1995, A&A, 3000, 675
Huchtmeier W. K., 1997, A&A, 319, 401
Huchtmeier W. K. Bohnenstengel H. D., 1975, A&A, 44, 479
Isobe T., Feigelson E. D., Nelson P. I., 1986, ApJ, 306, 490
Joseph R. D., Wright G. S., 1985, MNRAS, 214, 87
Kazes I., Proust D., Mirabel L. F., Combes F., Balkowski C., Martin J. M., 1990, A&A, 237, 1
Keel W. C., Kennicutt R. C., Hummel E., Van der Hulst J. M., 1985, AJ, 90, 708
Keel W. C., Wu W., 1995, AJ, 110, 129
Kennicutt R. C., ApJ, 1998, 498, 541
Kennicutt R. C., Roettiger K. A., Keel W. C., Van der Hulst J. M., Hummel E., AJ, 1987, 93, 1011
Klein U., 1982, A&A, 116, 175
Lawrence A., Rowan-Robinson M., Leech K., Jones D. H., Wall J. V., 1989, MNRAS, 240, 329
LaValley M., Isobe T., Feigelson E. D., 1992, BAAS, 24, 839
Lees J. F., Knapp G. R., Rupen M. P., Phillips T. G., 1991, ApJ, 379, 177
Lo K. Y., Gao Y., Gruendl R. A., 1997, ApJ, 475L, 103
Lutz D., Veilleux S., Genzel R., 1999, ApJ, 517, L13
Maiolino R., Ruiz M., Rieke G. H., Papadopoulos P., 1997, ApJ, 485, 552
Malin D. F., Carter D., 1980, Natur., 285, 643
Maloney P., Black H. J., 1988, ApJ, 325, 389
Martin J. M., Bottinelli L., Gouguenheim L., Dennefeld M., 1991, A&A, 245, 393
Martin M. C., 1998, A&AS, 131, 77
Mihos J. C., 1999, astro-ph/9903115
Mihos J. C., Hernquist L., 1996, ApJ, 464, 641
Mirabel I. F., Booth R. S., Johansson L. E. B., Garay G., Sanders D. B., 1990, A&A, 236, 327
Mirabel I. F., Sanders D. B., 1988, ApJ, 335, 104
Neff S. G., Hutchings J. B., Standord S. A., Unger S. W., 1990, AJ, 99, 1715
Norris R. P., Forbes D. A., 1995, ApJ, 446, 594
Planesas P., Colina L., Perez-Olea D., 1997, A&A, 325, 81
Read A. M., Ponman T. J., 1998, MNRAS, 297, 143
Richter O. G., Sackett P. D., Sparke L. S., 1994, AJ, 107, 99
Richter O. G., Huchtmeier W. K., 1991, A&AS, 87, 425
Rigopoulou D., Spoon H. W. W., Genzel R., Lutz D., Moorwood A. F. M., Tran Q. D., 1999, AJ, 118, 2625
Roberts M., Hogg D., Bregman J. N., Forman W. R., Jones C., 1991, ApJS, 75, 751
Sadler E. M., 1984, AJ, 89, 34
Sage L. J., Loose H. H., Salzer J. J., 1993, A&A, 273, 6
Sanders D. B., Scoviller N. Z., Soifer B. T., 1991, ApJ, 370, 158
Sanders D. B., Solomon P. M., Scoville N. Z., 1984, ApJ, 276, 182
Sanders D. B., Mirabel I. F., 1996, ARA&A, 34, 749
Smith D. A., Herter T., Haynes M. P., 1998, ApJ, 494, 150
Smith E. P., Kassim N. E., 1993, AJ, 105, 46
Soifer B. T., Sanders D. B., Madore B. F., Neugebauer G., Danielson G. E., Elias J. H., Lonsdale C. J., Rice W. L., 1987, ApJ, 320, 238
Solomon P. M., Sage L. J., 1988, ApJ, 334, 613
Solomon P. M., Downes D., Radford S. J. E., Barrett J. W., 1997, ApJ, 478, 144
Storchi B. T., Patroriza M. G., 1986, ApJ, 304, 305
Surace J. A., Mazzarealla J., Soifer B. T., Wehrle A. E., 1993, AJ, 105, 864

Schiminovich D., van Gorkom J. H., van der Hulst J. M., Kasow S., 1994, ApJ, 423, 101
Schweizer W., 1996, AJ, 111, 109
Schweizer W., Seitzer P., 1988, ApJ, 328, 88
Stanford S. A., Wood, Douglas O. S., 1989, ApJ, 346, 712
Terlevich A. I., Forbes D. A., 1999, in preparation
Theureau G., et al. 1998, A&AS, 130, 333
Tinney C. G., Scoville N. Z., Sanders D. B., Soifer B. T., 1990, ApJ, 362, 473
Toomre A., Toomre J., 1972, ApJ, 178, 623
Toomre A., 1977, 'The Evolution of Galaxies and Stellar Populations', edited by B. M. Tinsley and R. B. Larson (Yale University, New Haven), p. 401
Young J. S., Knezek P. M., 1989, ApJ, 347, L55
Young, J. S., et al. 1995, ApJS, 98, 219
Yun M. S., Hibbrand J. E., 1999, astro-ph/9903463
Yun M. S., Scoville N. Z., Knop R. A., 1994, ApJ, 430, 109
Wallin J. L., Struck-Marcell C., 1994, ApJ, 433, 631
Wiklind T., Combes F., Henkel C., 1995, A&A, 297, 643
Wrobel J. M., & Heeschen D. S., 1991, AJ, 101, 148

APPENDIX A1: NOTES ON INDIVIDUAL GALAXIES WITH NEW RADIO DATA

NGC 6769/70

This galaxy is strongly interacting with an equal mass spiral NGC 6770 with a bridge of stars connecting them. The optical centres of the two galaxies lie at RA = $19^h18^m22.6^s$, Dec.= $-60°30'03''$ and RA = $19^h18^m37.6^s$, Dec.= $-60°29'50''$ (J2000) respectively. Surface photometry of the galaxies is discussed in Storchi & Patroriza (1986). The radio contours at 4.79 GHz overlayed on the optical image of NGC 6770 are shown in Figure A1.

ESO 286–IG19

Imaging of ESO286–IG19 by Johansson (1991) reveals two tidal tails and a single $r^{1/4}$ like nucleus. This would tend to suggest a late stage merger. Comparison with the sequence of Keel & Wu (1995) suggests a dynamical stage of 1.5 (i.e $\approx 6\times10^8$ yrs). The radio contours at 4.79 GHz overlayed on the optical image of ESO 286–IG19 are shown in Figure A2.

NGC 1487

This system is in an early stage merger revealing two clear tails and two nuclei but sufficiently advanced to be one galactic body (e.g. Bergvall & Johansson 1995). It is slightly more evolved than NGC 4676 ("The Mice") but less so than NGC 4038/9 ("The Antennae"). The radio contours at 4.79 GHz overlayed on the optical image of NGC 1487 are shown in Figure A3.

ESO 034–IG11

Also known as the Lindsay–Shapley Ring (Lindsay & Shapley 1960). The asymmetric ring suggests an off–centre collision. It has been studied by Higdon & Wallin (1997). They found an optical bridge from the ring to the 'intruder' galaxy at RA = $06^h43^m26^s$, Dec. = $-74°15'29''$ (J2000). The optical nucleus of the perturbed galaxy is at RA = $06^h43^m06.7^s$, Dec.= $-74°14'16''$ (J2000). From the expansion rate of the ring in ESO34–IG11 the interaction occurred about 1.8×10^8 yrs ago ($H_0 = 75\,\mathrm{km\,s^{-1}\,Mpc^{-1}}$; Higdon & Wallin 1997). The radio contours at 4.79 GHz overlayed on the optical image of ESO 034–IG11 are shown in Figure A4.

NGC 7764A

The NGC 7764A system is an interacting triple system containing NGC 7764A NED2 (AM2350–410), 7764A NED3 to the south–east and 7764A NED1 to the north–west. The largest galaxy, NGC 7764A NED2, appears to be in the process of merging with NGC 7764A NED1 Borchkhadze et al. (1977) note the tidal material between these two galaxies. The smallest galaxy, NGC 7764A NED3 on the other hand shows only faint asymmetries in its outer optical isophotes. In this study, the NGC 7764A NED1/NED2 system is treated as a pre–merger, with two distinct galaxies present. The radio contours at 4.79 GHz overlayed on the optical image of NGC 7764A are shown in Figure A5.

ESO 138–IG29

Also known as the "Sacred Mushroom", this galaxy appears to be a young ring system formed by ESO138–IG30 as it passed through the disk of ESO138–IG29 less than 10^8 yrs ago (Wallin & Struck–Marcell 1994). Optical imaging and dynamical models of this system have been carried out Wallin & Struck–Marcell (1994) which suggest that ESO138–IG29 was originally an S0 galaxy. The radio contours at 4.79 GHz overlayed on the optical image of ESO 138–IG29 are shown in Figure A6.

ESO 341–IG04

This galaxy is probably at the very last stages of a merger. Its optical appearance is close to that of an elliptical galaxy (its surface brightness profile follows an $r^{1/4}$ law out to 5 effective radii), although it still contains a large amount of HI gas (Bergvall et al. 1989). It has one nucleus and one tail or plume, in addition to the prominent south–west loop. It appears to be more evolved than NGC 7252 but not quite at the end of the Keel & Wu (1995) merger sequence. The optical nucleus is at RA =$20^h41^m14.3^s$, Dec. = $-38°11'40''$ (J2000). The radio contours at 4.79 GHz overlayed on the optical image of ESO 341–IG04 are shown in Figure A7.

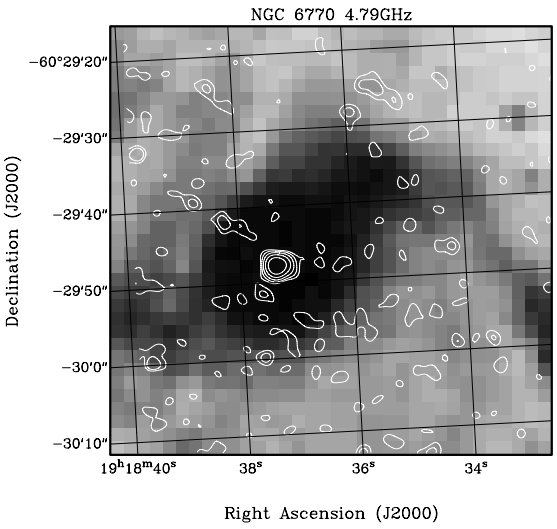

Figure A1. NGC 6770. Radio contours at 4.79 GHz (6 cm) overlayed on the Digital Sky Survey optical image (linear scale). The radio contours are logarithmically spaced between 0.05 mJy/beam and 1.35 mJy/beam using a logarithmic step of 0.48.

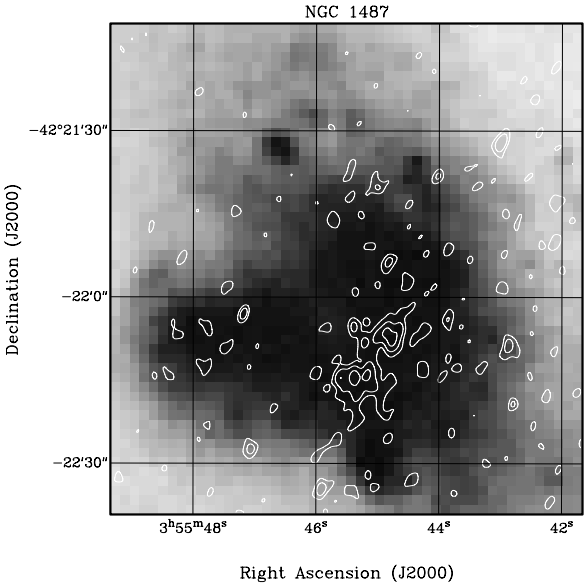

Figure A3. NGC 1487. Same as in Figure A1. The radio (4.79 GHz) contours are logarithmically spaced between 0.05 mJy/beam and 0.20 mJy/beam using a logarithmic step of 0.30.

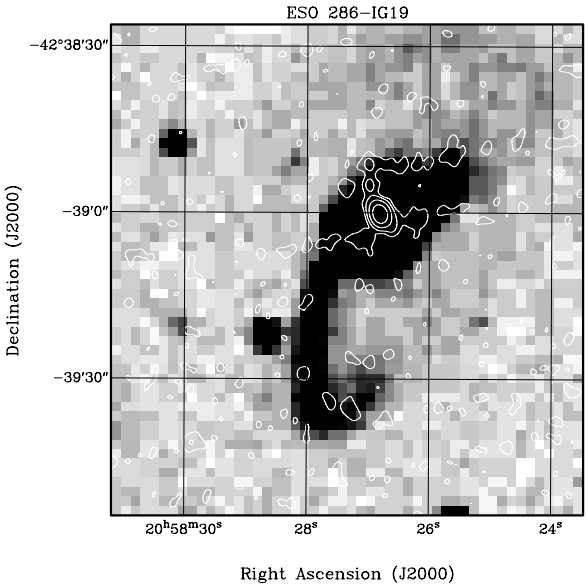

Figure A2. ESO 286-IG19. Same as in Figure A1. The radio (4.79 GHz) contours are logarithmically spaced between 0.06 mJy/beam and 3.84 mJy/beam using a logarithmic step of 0.60.

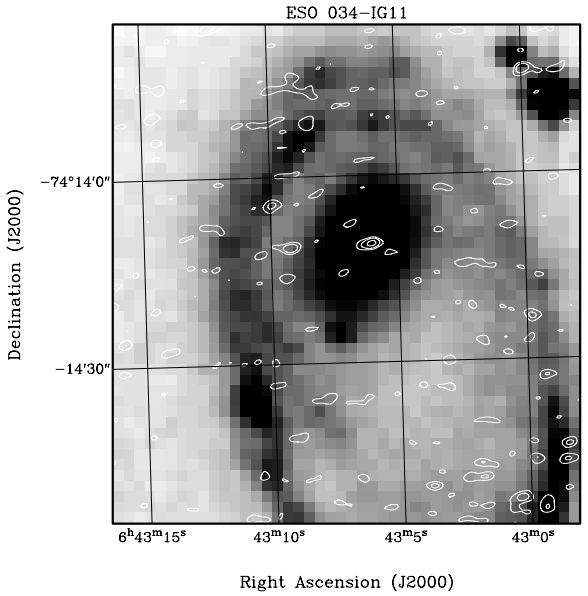

Figure A4. ESO 034-IG11. Same as in Figure A1. The radio (4.79 GHz) contours are logarithmically spaced between 0.05 mJy/beam and 0.20 mJy/beam using a logarithmic step of 0.30.

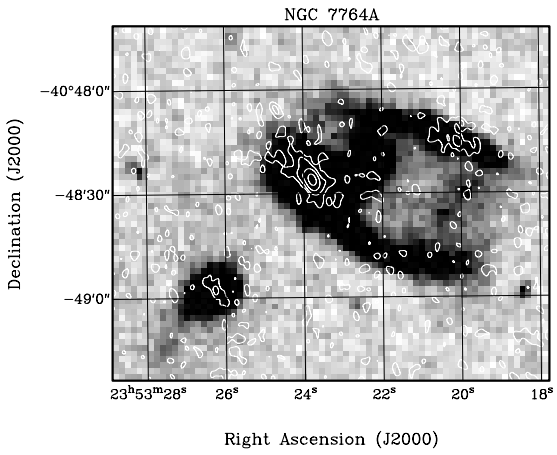

Figure A5. NGC 7764A. Same as in Figure A1. The radio (4.79 GHz) contours are logarithmically spaced between 0.07 mJy/beam and 1.89 mJy/beam using a logarithmic step of 0.48.

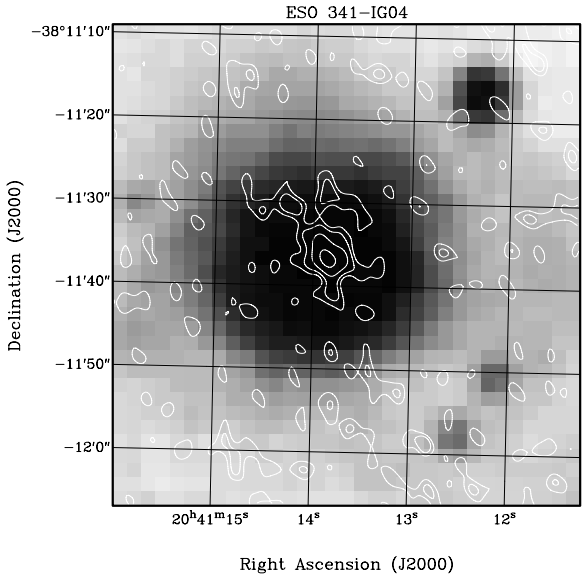

Figure A7. ESO 341-IG04. Same as in Figure A1. The radio (4.79 GHz) contours are logarithmically spaced between 0.05 mJy/beam and 0.40 mJy/beam using a logarithmic step of 0.30.

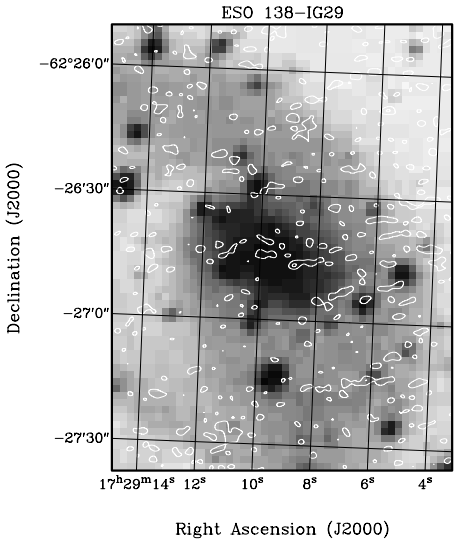

Figure A6. ESO 138-IG29. Same as in Figure A1. The radio (4.79 GHz) contours are logarithmically spaced between 0.07 mJy/beam and 0.21 mJy/beam using a logarithmic step of 0.60.